Journal of Raman Spectroscopy

RESEARCH ARTICLE OPEN ACCESS

Unveiling the Crystal Structure of Sanidine: A Polarized Raman and Ab Initio Simulation Exploration

Michele Cassetta[1,2] | Luca Bellucci[3] | Sabrina Nazzareni[4] | Francesco Vetere[5] | Marco Giarola[6] | Gino Mariotto[1]

[1]Department of Engineering for Innovation Medicine, University of Verona, Verona, Italy | [2]Department of Earth Science, University of Torino, Torino, Italy | [3]Istituto-Nanoscienze del Consiglio Nazionale delle Ricerche (CNR-NANO) at NEST, Scuola Normale Superiore (SNS), Pisa, Italy | [4]Dipartimento di Scienze Chimiche, della Vita e della Sostenibilità Ambientale, Università di Parma, Parma, Italy | [5]Department of Physical Sciences, Earth and Environment, University of Siena, Siena, Italy | [6]Technological Platforms Center (CPT), University of Verona, Verona, Italy

Correspondence: Michele Cassetta (michele.cassetta@univr.it)

Received: 20 February 2025 | **Revised:** 20 August 2025 | **Accepted:** 22 August 2025

Funding: This study was supported by the following: L.B.: Project PRIN 2022–Cod. 202278NHAM (PE11) CHERICH-C "Chemical and electrochemical energy storage materials from organic wastes: the treasure hidden in C based materials"–CUP B53D23008590006, funded by the European Union–Next Generation EU in the context of the Italian National Recovery and Resilience Plan, Mission 4, Component 2, Investment 1.1, "Fondo per il Programma Nazionale di Ricerca e Progetti di Rilevante Interesse Nazionale (PRIN)"; M.C., M.G., and G.M.: European Union's Horizon 2020 Research and Innovation Program under Grant agreement No. 689868; F.V.: Piano di Sostegno alla Ricerca 2022 per finanziamenti a progetti di ricerca Curiosity-driven (UniSi, F-CUR CREAMI).

Keywords: ab initio calculations | K-feldspars | Raman spectroscopy | sanidine | vibrational analysis

ABSTRACT

Sanidine, the high-temperature polymorph of potassic feldspar, plays a crucial role in the formation of volcanic rocks. Despite extensive research, the complexity of K-feldspar polymorphs remains poorly understood. This study, by combining polarized Raman spectroscopy with ab initio calculations, aims to definitively assign the vibrational modes predicted by theory to those observed experimentally. A sanidine megacryst from the rhyo-dacite sub-intrusive body of Terlano (Ora mega-caldera complex, Southern Alps, Italy) was used for this purpose. Polarized Raman spectra were collected in six scattering geometries, allowing for precise mode selection within the 40–1200 cm^{-1} range. Our vibrational analysis, based on density functional theory, provides wave-numbers and normal modes having trends that largely align with experimental data. The combination of experimental data and theoretical calculations also indicated that the models in which aluminum is located at the T_1 tetrahedral site are more stable than those with aluminum at the T_2 site. This finding provides further insight into the order–disorder phase transition in K-feldspar, a phenomenon that is difficult to replicate under laboratory conditions. These results further improve our understanding of the relationship between theoretical models and the actual spectral characteristics of this disordered mineral. The full assignment of normal modes presented here lays the foundation for future studies of phase transitions in K-feldspars using Raman spectroscopy.

1 | Introduction

Feldspars are widespread in many different geological environments and account for approximately 50%–60% of the Earth's crust. The occurrence, geochemistry, and petrological characteristics of feldspar are thus of fundamental importance for the description of geological processes (i.e., by exsolution features, by two-feldspar geothermometry [1], by polymorphism and isomorphism [2]). In particular, K-feldspar, $KAlSi_3O_8$, is the most stable among the three end-members of feldspars (orthoclase [K], albite [Na], and anorthite [Ca]). K-feldspar high stability makes this phase dominant in the crust and upper mantle [3] Moreover, is one of the few potassic phases stable at high pressure (k-hollandite [4], KK-richterite [5], phase-X [6]); thus, it

---

https://doi.org/10.1002/jrs.70043

can be considered an important candidate for transporting potassium deep into the Earth mantle (i.e., by the way of a cold subduction zone [3]). In magmatic environments, K-feldspar is characterized by three polymorphs, sanidine, orthoclase, and microcline, which range from high to low temperature stability. The temperature-dependent K-feldspar polymorphism could therefore be used to reconstruct magmatological processes [2]. Monoclinic mega K-feldspars of volcanic origin are peculiar to magmatic systems. They are among the most enigmatic mineral structures found in volcanic environments, displaying highly cations-disordered structures that may record the long-term thermal history of volcanic rocks.

Sanidine is the high temperature polymorph, high-sanidine, with space group symmetry $C2/m$, and each unit cell ($a = 8.5$ Å, $b = 13.0$ Å, $c = 7.2$ Å, $\hat{\beta} = 116°$, respectively; [7]) contains 4 formula units $KAlSi_3O_8$. Feldspars are framework structures of 3D tetrahedra forming building blocks of 4-membered tetrahedra rings. The large cations (Na, Ca and K) are located in a special position on the (010) mirror plane inside the irregular cavity formed by tetrahedra rings and coordinated by 8 oxygens. The cavities are formed by four-membered rings of corner-sharing tetrahedra arranged in two sets of equivalent tetrahedral sites T_1 and T_2 for 16 Si and Al. Each tetrahedral apex points in $+a$, $+a$, $-a$, $-a$ directions to form the so-called crankshaft chain, where a center of symmetry relates opposing tetrahedra (Figure 1). The chain is linked through the bonds between T_2 and the O_{a2} oxygen along b direction to form sheets which in turn are bonded through T_1 and O_{a1} along c direction. This configuration is responsible for good cleavage parallel to the (001) plane. The final 3D structure is a cage-like network having a centered cell, which is twice as large as the primitive cell, with an average composition of $Al_{1/4}$ and $Si_{3/4}$.

What characterizes the K-feldspar polymorphic series is an order–disorder degree of Al atoms over the two sets of T sites.

The ordering process depends on kinetics and is strongly influenced by the crystallization temperature (T_c) on the displacive phase transition [8–10]. The degree of order can be directly estimated by observing the Al distribution over the T sites. The higher the T_c (close to the melting point), the higher the disorder; Al is random distributed within T_1 ($T_{1o} = T_{1m}$) and T_2 ($T_{2o} = T_{2m}$), forming sanidine with monoclinic symmetry. Decreasing temperature (and cooling rate), T_1 site became the most energetic favorable site for Al, which mainly ordered there, giving birth to orthoclase, the partially ordered monoclinic polymorph of the series. A further decrease of T_c causes a complete Al order at T_1 site; the mirror symmetry is lost, and the two tetrahedral sites become four symmetrically distinct ones (T_{1o}, T_{1m}, T_{2o}, T_{2m}). The stable phase is the triclinic microcline [11]. The order–disorder polymorphism is a kinetic process; thus, it depends on the cooling rate, a parameter extremely useful to describe the geology of host rocks (i.e., order–disorder of Mg-Fe on pyroxene [12], Al-Si in K-feldspar [13]) that can eventually be related in a second instance to magma ascent, for example, [14–17]. In this framework, an interesting task is to characterize feldspar polymorphs with techniques like Raman spectroscopy, which, unlike X-ray diffraction or TEM, can be more easily used in ordinary rocks characterization. However, any attempt to establish a relationship between variations in the vibrational spectrum as function of composition, temperature, or pressure—within the context of crystal structure, requires detailed knowledge of the vibrational characteristics of each mode. The importance of peak assignment goes far beyond characterizing the spectrum of a given geological compound, [18–20]. Indeed, the limited number of bands in sanidine indicates a remarkable complexity due to its disordered structure [21]. Thus, the need to classify (order the disorder) the modes of such a complex mineral, which constitutes about 60% of the Earth's crust rocks, is still an open challenge on a broadly multidisciplinary scale.

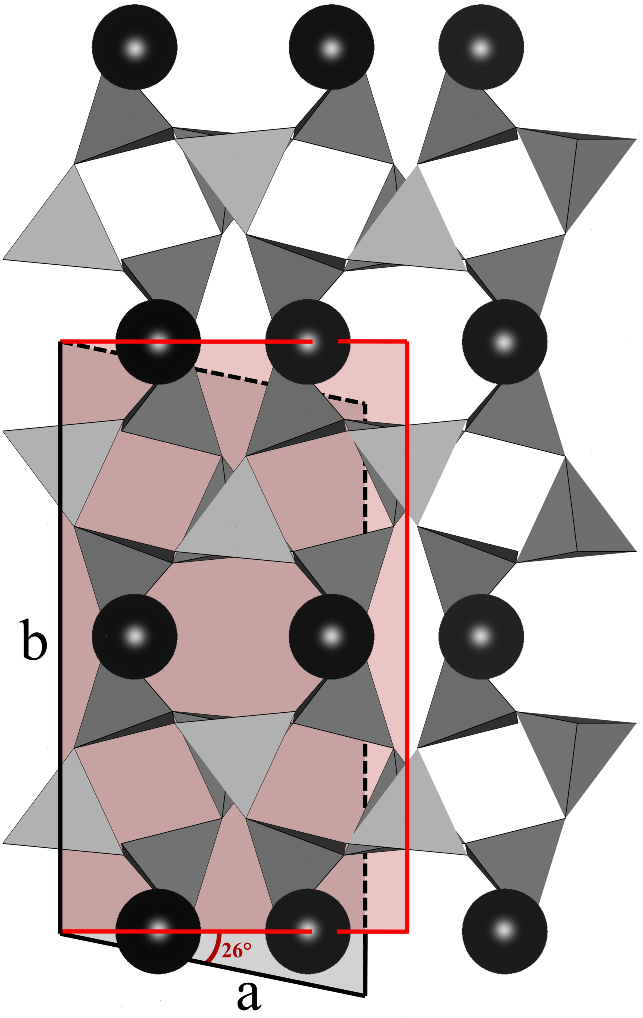

FIGURE 1 | Sanidine structure view perpendicular to c crystallographic axis. Tetrahedra T_1 in light grey and T_2 in dark grey are reported, potassium atoms are the black spheres. The red area indicates the plane perpendicular to the c axis, while the area within black lines represents the crystallographic $a-b$ plane tilted by 26° relative to the red plane and 116° relative to the c axis.

In this study, our aim was to unravel the experimental and simulated Raman spectrum of a natural sanidine and definitely ascribe the modes to those theoretically predicted.

2 | Material and Methods

The studied sample is a megacrystal from the rhyo-dacite subintrusive body of Terlano (Permian Ora mega-caldera complex, a super volcano in the Southern Alps, Italy), whose hosting rock composition (sample Ora) is reported in Ref. [22].

2.1 | Electron Microprobe

The analysis was focused only on the micro domain of the inner core of the megacrystal, in order to avoid as much as possible chemical heterogeneities (zonation) or secondary mineral crystallization. Chemical composition (Table 1) was retrieved by a CAMECA SX100 electron microprobe analyzer (University of Hannover) whose beam was set with a current of 15 nA and focused on a spot having 1-μm diameter. The counting time on peak was 15–20 s (7.5–10 s for background) for each element. We used the following standards for Kα X-ray line calibration: albite for Na, orthoclase for K, wollastonite for Si and Ca, alumina for Al, anatase for Ti, and MgO for Mg.

2.2 | Single Crystal X-Ray Diffraction

Crystal core fragments (S_a and S_b) from the sanidine megacrystal were oriented by single-crystal X-ray diffraction (SC-XRD) on an Xcalibur diffractometer (Rigaku) equipped with a CCD camera and using graphite monochromatized MoKα radiation (University of Perugia). Samples were mounted on a goniometric head to carry out a data collection up to $\theta = 31°$ and measure the unit cell parameters. We also evaluated the crystalline quality of the fragments by the rocking curve of a selection of reflections. Samples were thus oriented by the crystallographic planes (100) and (010) by applying the orientation matrix. Each crystal was then mounted on a glass plate using adhesive and polished for polarized Raman analyses.

2.3 | Raman Spectroscopy

The polarized micro-Raman spectra were recorded at room temperature on the oriented K-feldspar grain (500 μm) in backscattering geometry by means of a triple-axis monochromator (Horiba-Jobin Yvon, T-64000) in a double subtractive single configuration set up with a holographic grating (1800 lines/mm) interfaced to a charge coupled device (CCD) detector cooled by liquid nitrogen (1024 × 256 pixels). The exciting radiation was provided by a mixed Ar-Kr ion gas laser (Spectra Physics Satelite 2018 RM), tuned at 514.5 nm, which allowed for a resolution of about 0.6 cm^{-1}/pixel (University of Verona). The laser beam was focused onto a spot of about 2 μm in size by using a long working distance 50× objective with N.A. = 0.50, while the power on the sample surface was fixed at 10 mW [23]. The sample was mounted on a micromanipulator and monitored with a camera implemented in the same microscope objective used to collect the scattered radiation [24]. This setup allows not only for an optical inspection to focus the laser beam, but also for an optimal orientation of the sample. According to the Porto's notation [25], the scattering configuration can be written as $\bar{Z}(XY)Z$, where $\bar{Z}$ and Z are the propagation direction of the incident and scattered light, while X and Y are the polarization direction of the incident and scattered light, respectively. By defining X, Y, Z as laboratory axes coordinate system, we fixed Z as the optical axis of the objective used to collect the scattered radiation, and jointly liable to the crystallographic axes *a*, *b*, *c*. For each crystallographic axis, 4 measurements were performed by probing according to the following geometry: $\bar{Z}(XX)Z$, $\bar{Z}(YY)Z$, $\bar{Z}(XY)Z$, and $\bar{Z}(YX)Z$. Raman spectra were collected in a backscattering configuration with the laser focused onto the sample surface. The penetration depth under our conditions is estimated to be 1.5 μm, minimizing the optical path with concomitant reduction of the potential depolarization effects in this birefringent monoclinic crystal. To optimize the orientation, the sample was mounted on a micromanipulator allowing for fine rotation and tilting. The position was adjusted to maximize the intensity extinction or enhancement of A_g and B_g symmetry modes, based on relative intensity ratios across polarization configurations. This procedure allowed us to approximate the symmetry assignments with acceptable reliability, despite the optical anisotropy of the crystal.

TABLE 1 | Chemistry analysis of the sanidine megacrystal from Terlano.

Oxide	wt%
SiO_2	66.47 (48)
Al_2O_3	18.13 (36)
Na_2O	4.39 (8)
K_2O	11.01 (9)
Tot.	100

Note: In brackets are reported 2σ.

2.4 | Modeling and Computational Details

All simulations were performed with CP2K software package [26, 27]. Using the mixed Gaussian and plane waves (GPW) approach [28] at the density theory level. The base sets were the optimized triple ζ plus two sets of polarization function (TZV2P-MOLOPT) with PBE optimized Goedecker-Teter-Hutter (GTH) pseudopotentials for all atoms [29, 30] to treat the core electrons. The energy cutoff for the auxiliary plane-wave basis was set to 1200 Ry. Standard Perdew–Burke–Ernzerhof exchange and correlation functional [31] (PBE), its reparameterization for solids [32] (PBEsol), and the so called PBE0 hybrid functional model [33], which mixes PBE exchange energy and Hartree–Fock exchange energy, were used. All simulations take advantage of the Grimme D3 correction to account for van der Waals interactions [34]. The calculation with the hybrid PBE0 functional is computationally more demanding than the calculation with the generalized gradient approximation (GGA) functionals such as PBE and PBEsol [27]. To enable hybrid PBE0 calculations at a cost comparable to that of GGA functionals, the auxiliary density matrix method [35, 36] (ADMM) was used for the Hartree-Fock exchange to perform calculations with this hybrid functional. The auxiliary basis sets were pFIT3 for the Si and O atoms and FIT7 for K and Al atoms. The Brillouin zone was sampled at the Γ point.

Geometry and cell optimizations were carried out using the Broyden-Fletcher-Goldfarb-Shanno (BFGS) minimization algorithm as implemented in CP2K. The convergence criteria were

10E-6 Bohr for displacements and 10E-6 Hartree/Bohr for forces, respectively. Specific measures were not adopted to constrain the $C2/m$ symmetry of the unit cell during the calculations. The unit cell for sanidine was modeled from the experimental data reported in the work of [37]. The models SL1, SL2, SL3, and SL4 (Figure 3) were constructed by exchanging two Si atoms with two Al atoms while maintaining the $C2/m$ symmetry of the pristine unit cell. The optimized geometries were then subjected to the calculation of vibrational frequencies, Raman intensity and normal modes using the vibrational-analysis module within CP2K. The calculated spectra were plotted using the Lorentzian band shape with full width at half maximum (FWHM) set to $12\,\text{cm}^{-1}$.

3 | Results

3.1 | Chemical Composition and Crystal Structure

The studied sanidine megacrystal is a solid solution of the orthoclase (Or: $KAlSi_3O_8$) and albite (Ab: $NaAlSi_3O_8$) end-members with $Or_{62}Ab_{38}$ proportion (Table 1). This mirrors a moderate substitution of Na for K.

The lattice parameters measured for the crystal core fragments (S_a and S_b) of the sanidine megacrystal are reported in Table 2. The lattice parameters of S_a and S_b sanidine differ within the range of experimental errors and are consistent with the values reported in literature [7, 11].

3.2 | Raman Spectroscopy

All the peaks and bands observed in the Raman spectra can be identified according to the classification of the vibrational modes done in Ref. [19], as follows: (*i*) the spectral range below $400\,\text{cm}^{-1}$ is linked to the rotation-translation modes of the four-membered rings and cage-shear modes, respectively; (*ii*) the range $450–520\,\text{cm}^{-1}$ (most intense populated peaks) is associated with the ring-breathing modes of the four-membered tetrahedral rings; (*iii*) peaks of mid to weak intensity in the $700–900\,\text{cm}^{-1}$ region correspond to the deformation modes of the tetrahedra; (*iv*) bands in the $900–1200\,\text{cm}^{-1}$ region are attributed to the vibrational stretching modes of the tetrahedra. Figure 2 shows six pairs of polarized spectra, both in parallel $\overline{\text{Z}}(\text{XX})\text{Z}$ and in crossed $\overline{\text{Z}}(\text{XY})\text{Z}$ excited along each crystallographic axis.

Factor-group analysis of sanidine shows that 75 optic modes are distributed among the following symmetry species: $\Gamma_o = 20A_g(R) + 19B_g(R) + 17A_u(IR) + 19B_u(IR)$, where R and IR refer to Raman and infrared active modes, respectively. The tensor components of the Raman active modes are [38]:

$$A_g = \begin{pmatrix} \alpha & 0 & \delta \\ 0 & \beta & 0 \\ \delta & 0 & \gamma \end{pmatrix} \quad B_g = \begin{pmatrix} 0 & \varepsilon & 0 \\ \varepsilon & 0 & \zeta \\ 0 & \zeta & 0 \end{pmatrix}$$

Table 3 reports the peak positions as centroid upon Lorentzian fitting. In order to make a comparison between our outcomes and those from literature, we averaged the peak positions identified in spectra where the mode was symmetry permitted (i.e., in $\overline{\text{Z}}(\text{XY})\text{Z}$ spectra for B_g modes and $\overline{\text{Z}}(\text{XX})\text{Z}$ spectra for A_g modes) (Table 3). The relative intensities of the different modes in the various scattering configurations are referenced to the intensity of the strongest A_g mode at $516\,\text{cm}^{-1}$, while the assignment of the spectral features is carried out in terms of Raman scattering matrix components (1), where:

(α) The A_g modes here consist of a set of bands peaked at 408, 726, 762, and $1123\,\text{cm}^{-1}$. The first one shows both the α and β components. These modes belong to the vibrational stretching and bending motions within the silicate structure with respect to the a axis.

(β) The A_g modes are characterized by several distinct peaks such as: 64, 108, 125, 458 (which is particularly notable for being a well-resolved peak in the spectrum), 755, 1013, and $708\,\text{cm}^{-1}$. As stated above, the peak at $408\,\text{cm}^{-1}$ also displays the α character of the scattering matrix.

(γ) The A_g modes lying in this component include the following peaks: 146, 170, 1029, 1050, 1132, and $286\,\text{cm}^{-1}$, which are significantly more intense than the β component, highlighting its prominence in the γ component.

(δ) The A_g modes include: 369 and $408\,\text{cm}^{-1}$. This mode provides insights into the cage-shear dynamics within the structure.

(ε) The B_g modes of this component include: 63, 108, 173, 199, 774, and $1000\,\text{cm}^{-1}$ and the very weakly detected mode at $321\,\text{cm}^{-1}$.

TABLE 2 | Experimental (Exp.) and theoretical (DFT, such as SL1, SL2, SL3, and SL4 models).

	Exp.		DFT			
	S_a	S_b	SL1	SL2	SL3	SL4
a	8.551(13)	8.539(14)	8.610	8.643	8.643	8.610
b	12.972(17)	12.988(15)	13.094	12.863	12.863	13.094
c	7.200(8)	7.196(13)	7.106	7.183	7.183	7.106
$\hat{\beta}$	116.14(13)	116.02(17)	115.6	116.02	116.02	115.6
E			−358.3987	−358.3990	−358.3990	−358.3987

Note: Cell parameters a, b, and c are in Å, $\hat{\beta}$ angle in degrees. $\hat{\alpha}$ and $\hat{\gamma}$ are 90°. Energy (E) is expressed in eV per atom (eV/n).

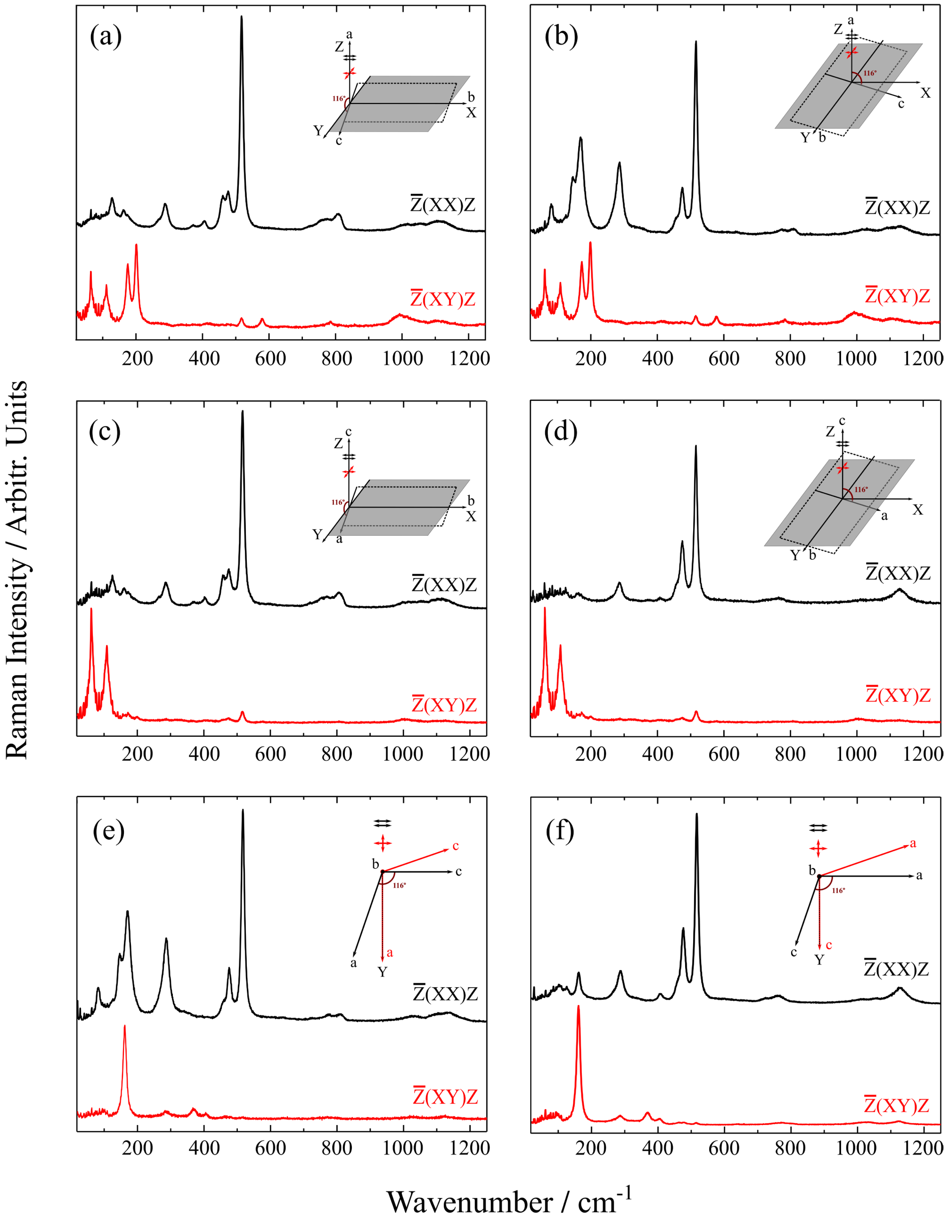

FIGURE 2 | Polarized spectra (black for $\overline{Z}(XX)Z$ and red for $\overline{Z}(XY)Z$) excited along each crystallographic axis. The insets represent the arrangement of the polarization configurations (parallel black and crossed red arrows) whilst *a*, *b*, and *c* are the crystallographic axes and X, Y and Z the lab axes. Grey areas indicates the plane perpendicular to the *a*-axis (a, b) and *c*-axis (c, d).

(ζ) The B_g modes here are characterized by the following peaks: 162, 580, 640, 774, 782, 990, 1023, and 1100 cm^{-1} and that, although extremely weak, at 369 cm^{-1}.

It follows that from the structure of the Raman tensor, the differences in the intensities of the lines within each of the $\overline{Z}(XX)Z$ and $\overline{Z}(XY)Z$ spectra must be attributed to the contributions of the various components of the tensor. However, since the symmetry in the monoclinic system is locally violated by the Al-Si disorder, the presence of peaks at the same frequencies (although with different intensities) in all the spectra must be expected. This can blur the distinction among A_g and B_g modes, as the selection rules become only approximately valid due to symmetry lowering, mode overlap, and local disorder. As a matter of fact, with $\widehat{\beta}$ of about 116°, at least one of the *a* or *c* axes is tilted relative to the optical axis, so light polarized along these directions may not retain its polarization within the crystal, making polarization conditions only partially satisfied under standard micro-Raman configurations.

3.3 | Modeling and Calculated Vibrational Spectra

Minimized models for sanidine, namely, SL1, SL2, SL3, and SL4, are shown in Figure 3. The cell parameters calculated exploiting the density functional PBE0 are reported in Table 2 and show good agreement with the experimental values; SL1 and SL4 show parameters similar to those of SL2 and SL3. The deviation between the calculated average energies per atom for

TABLE 3 | Experimental (exp.) and calculated (SL1, SL2, SL3 and SL4) bands classified according to their symmetry properties: A_g and B_g.

No.	A_g					B_g				
	Exp.	**SL2**	**SL3**	**SL1**	**SL4**	**Exp.**	**SL2**	**SL3**	**SL1**	**SL4**
1	82	82	79	82	80	63	50	45	51	56
2	99	93	92	89	88	108	114	115	104	105
3	105	100	100	95	94	162	176	177	173	175
4	125	131	132	122	118	173	187	185	182	183
5	146	146	148	138	140	199	244	243	237	237
6	170	182	179	181	179	321	320	321	312	311
7	265	275	274	270	270	369	378	378	369	369
8	286	287	289	281	280	404	397	399	386	388
9	408	408	407	408	409	463	438	439	431	432
10	458	438	436	431	432	479	505	504	494	495
11	475	470	470	471	472	580	582	583	578	576
12	516	528	529	415	416	640	663	665	657	657
13	726	759	759	735	734	774	715	715	711	711
14	755	791	791	774	774	782	774	774	756	758
15	762	793	793	785	786	805	805	806	802	804
16	808	817	818	821	822	990	990	990	973	974
17	1013	1030	1030	1028	1028	1000	1001	1002	984	985
18	1054	1049	1050	1053	1053	1023	1024	1024	1020	1020
19	1123	1152	1152	1155	1153	1100	1135	1135	1149	1149
20	1132	1175	1176	1204	1205					

Note: The error on the experimental position is about 0.6 cm^{-1}.

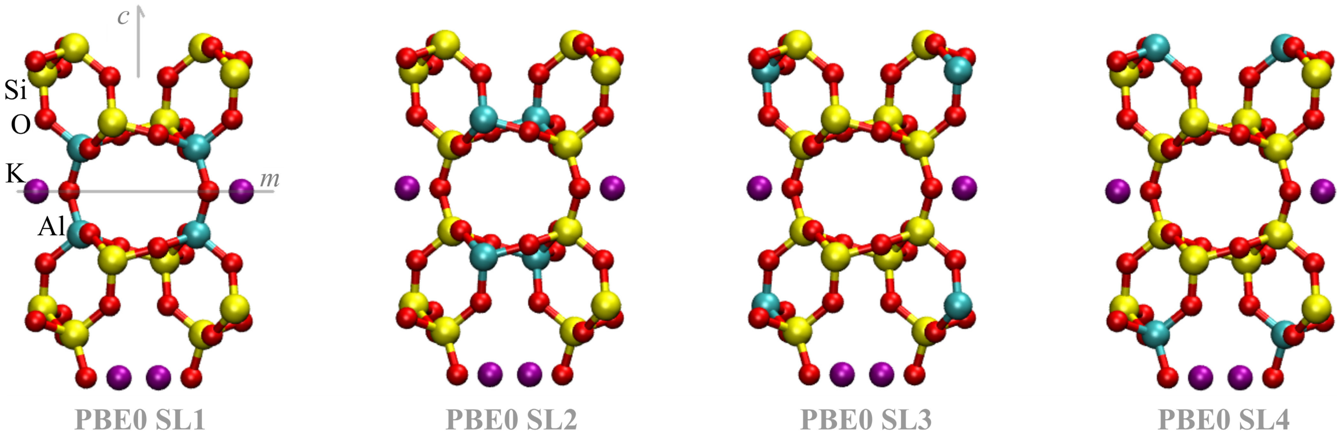

FIGURE 3 | From left to right: SL1, SL2, SL3, and SL4 optimized with PBE0. Al cyano, K purple, Si yellow, and O red.

each model is negligible, as it remains within a 1 meV threshold (Table 2). However, SL2 and SL3 are slightly more stable than SL1 and SL4. PBE and PBEsol density functionals yield the largest differences in cell parameters with respect to the experimental data (see Table S1), while the energy per atom (Table S2) indicates a slightly higher stability for SL2 and SL3 compared to SL1 and SL4, as in the case of PBE0.

The Raman wavenumbers calculated using the PBE and PBEsol functionals are underestimated as detailed in Figure S1. Raman spectra derived from the computed wavenumbers and intensities using the PBE0 functional exhibit trends comparable to experimentally reported spectra (see Figures 4 and S2), but it is imperative to consider that experimental spectra may be influenced by the presence of additional elements as well as

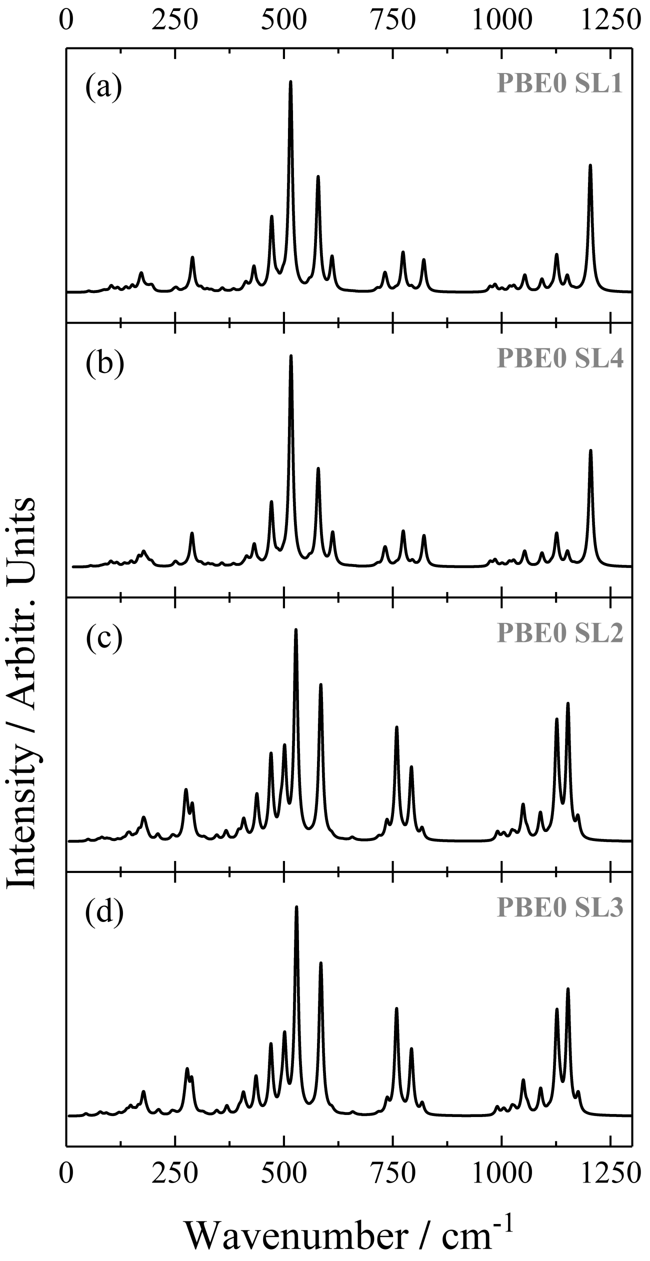

FIGURE 4 | Reconstructed Raman spectra from wavenumbers and intensity evaluated with PBE0 functional and models SL1 and SL4 (a, b) and SL2 and SL3 (c, d).

complex, random crystalline structural domains when comparing experimental data with computational data. Therefore, only the wavenumbers corresponding to distinct normal modes with unambiguous symmetry and the highest calculated intensity are examined in this section (see Section S3 for more details).

Notably, the spectra for SL1 and SL4 models (SL14) in Figure 4a,d and those for SL2 and SL3 models (SL23) in Figure 4b,c show similar features, with significant overlap (see also Figure S2 for a direct comparison). The main peaks around 516 cm^{-1} for SL1 and SL4 correspond to the most intense peak observed in the experimental spectra. This peak exhibits A_g symmetry, as indicated by its corresponding normal mode, specifically normal mode 1 (NM1), in Table S3. SL2 and SL3 exhibit the same mode and symmetry, but with a 13 cm^{-1} blue shift, appearing at approximately 528 cm^{-1}.

The second intensity peak in SL14 models at 1200 cm^{-1} does not appear in the experimental spectra or in the calculated spectra for SL23 (see Figure 4 for a direct comparison). The normal modes corresponding to these peaks (Table S3, NM2) exhibit a non-negligible Si-O stretching component oriented along a and show A_g symmetry. The similar A_g normal mode for SL23 is 1176 cm^{-1} (weak peak). The decrease in the wavenumber is due to the exchange of Si atoms with Al atoms in equivalent oriented Al-O stretching (Table S3, NM2).

The decrease of this specific peak in SL23 is due to the presence of Al in the T_1 site. In contrast, SL14 lacks this feature because Al is in the T_2 site, accounting for the differences between the two vibrational spectra. The lack of activity around 1200 cm^{-1} in the experimental spectra may be due to the absence of Al at the T_2 site in the natural samples. This highlights that models SL2 and SL3, with Al in the T_1 site, are more representative of the real case than SL1 and SL4, where Al is at the T_2 site.

The medium intensity peaks and the two minor peaks observed in the SL23 models within the 1000–1160 cm^{-1} range, as well as the less pronounced peaks in the SL14 models, are all attributable to Si/Al-O-related stretching vibrations. These peaks can be associated with the A_g and B_g peaks observed between 900 and 1200 cm^{-1} that are attributed to the vibrational stretching modes of the tetrahedra.

Notably, the SL23 models show a higher degree of congruence with the experimental spectra, primarily due to the absence of the band at 1200 cm^{-1}. In addition, the medium intensity peaks detected within the 700–850 cm^{-1} range further corroborate this observation, indicating that the SL23 models are more representative of the experimental structures. SL14 exhibits three medium-intensity peaks at 821, 774, and 731 cm^{-1}, whereas SL23 shows two medium/high-intensity peaks at 793 and 759 cm^{-1}, along with smaller peaks at 736 and 818 cm^{-1} (see Figure S2), which align more accurately with the broad band between 720 and 800 cm^{-1} in the experimental data (Figure 2). The major peaks observed at 793 and 759 cm^{-1} in the SL23 models are attributed to Si-O-Si bending modes (refer to NM3,4 in Tables S3 and S2) and both show A_g symmetry. These peaks and normal modes are similar to those found in the SL14 models but at different wavenumbers (NM5,6,7, Table S2).

Each model shows a prominent peak around 580 cm^{-1}. Specifically, the SL14 models show peaks at 579 cm^{-1} with a relatively less intense peak at 612 cm^{-1}, while the SL23 models show peaks at 585 cm^{-1} (NM8, Table S3).

A comprehensive attempt to compare the calculated wavenumbers and normal mode representations of the SL23 models with respect to the experimental wavenumbers can be found in Table S4 and depicted in Figure S3, while the corresponding wavenumbers are reported in Table 3.

4 | Discussion

The main contributions to the atomic motions derived from our Raman tensor analysis were validated with the eigenvectors of the relevant normal modes after having updated previous work attributions [20, 22, 38–41]. We have highlighted the four regions in the Raman spectrum where the vibrational modes are produced by the cage-shear and rotation-translation of the rings at low wavenumbers, and, increasing the wavenumbers, by the ring-breathing, the tetrahedral deformation and by the vibrational stretching of tetrahedra. Generally, the comparison between the experimental (exp.) and the calculated values (SL2 and SL3) in Table 3 for A_g and B_g modes reveals notable differences in the magnitude of discrepancies across the two symmetries (see also Table S4). For the A_g modes, the experimental values generally align closely with the calculated ones, particularly at lower wavenumbers. In contrast, the B_g mode demonstrates greater divergence from the experimental spectra. In particular, models SL2 and SL3 frequently overestimate the experimental results (see Tables 3 and S4). Overall, the A_g mode shows a better correlation between experimental and calculated values, while the B_g mode exhibits greater variability and larger discrepancies.

In the following, we discuss the four regions separately.

4.1 | Cage–Shear and Rotation–Translation Modes of the Rings (Below 400 cm^{-1})

Modes in the region below 400 cm^{-1} are produced by the cage-shear and by a combination of rotation-translation of the tetrahedra rings.

In the low wavenumbers region (below 200 cm^{-1}) modes are characterized by the translation of K in the structure. Potassium is the larger cation in the structure and is sited in the mirror plane inside the large cages defined by the tetrahedral framework. In this configuration K cannot simply translate parallel to the *a* axis (wavenumber at 82 cm^{-1} and the assigned normal mode 6 [ANM-6] in Table S4), but the translation can also be associated to rigid rotation of the SiO_4 tetrahedra (mode at 63 cm^{-1}) and with additional participation of the AlO_4 tetrahedra (mode at 99 cm^{-1}). Thus, the rotation of T_2 and T_1 tetrahedra is expected to originate modes at 105, 108, 125, and 146 cm^{-1}. The part of the region between 200 and 400^{-1} consists of rotation and deformation of the tetrahedra modes. The tetrahedra rotations produce a mode at 286 cm^{-1}, while the mode at 265 cm^{-1} is due to the rigid rotations of the SiO_4 tetrahedra and deformation of the AlO_4 tetrahedra, where the Al and O atoms move significantly. The deformations of the tetrahedra (involving mostly the bending of Al–O–Si and Si–O–Si bonds) produce modes at 369, 404, and 408 cm^{-1}.

In the modes at 105, 108, 125, and 146 cm^{-1} related to the rotations of the tetrahedra T_2 and T_1, with additional translation of the K^+ cations, the contribution to the motion is higher at 146 cm^{-1} than at 105 cm^{-1}. Interestingly, the mode at 125 cm^{-1} can be classified as A_g since we observe both as shoulder in the $\bar{Z}$(XX)Z spectra (selecting only A_g) and as single peak in c (bb)c and b (aa)b.

4.2 | Ring-Breathing Modes (450–520 cm^{-1})

In the 450–520 cm^{-1} region, the modes are related to the ring-breathing mainly by deformation of the tetrahedra. The mode at 458 cm^{-1} is produced by the motion of Si atoms contribute, in particular, in the $T_{2(0)}$ tetrahedra. The mode at 475 cm^{-1} is a cage-breathing mode assigned mainly to the bending of O–Si–O and Si–O–Si (or Al). The mode at 516 cm^{-1} is due instead to the bending deformation of the Al–O–Si and Si–O–Si bonds (NM1, in Table S3, ANM-90 in Table S4).

It is worth noting that in the mode at 516 cm^{-1}, the motion is mainly distributed on the oxygen atom along a line bisecting the T–O–T angle, maintaining the T's core cations virtually motionless. Comparison between the a (cc)a spectrum (the $\bar{Z}$(XX)Z configuration in Figure 2b) and b (ac)b (the $\bar{Z}$(XY)Z) configuration in Figure 2e,f) in the region between 450 and 550 cm^{-1}, where we have the filtering of the A_g mode at 515 in b (ac)b, but at 463 and 479 cm^{-1}, two B_g modes are distinctly highlighted compared to the A_g mode at 475 (which falls right in the middle between the two modes).

4.3 | Deformation Modes (570–900 cm^{-1})

In the 570–900 cm^{-1} region, the modes are related to the deformation of tetrahedra, the forming framework of the feldspar structure. We could assign different contributions of the two equivalent T sites, T_1 and T_2, in which the ordering of Si-Al occurs during the phase transition. The mode at 580 cm^{-1} is assigned to the deformation of the tetrahedra, with a strong contribution of T_1. The bending deformation of the tetrahedra, also characterized by the statistical disorder of aluminum distribution, are between 640 and 726 cm^{-1}. The mode at 774 cm^{-1} is assigned to the bending deformation of T_2 tetrahedra. The deformation of the four tetrahedra is recorded by the modes at 782 and 808 cm^{-1}, with the T_1 tetrahedra that make a major contribution to the motion at 782 cm^{-1}.

4.4 | Vibrational Stretching Modes (900–1200 cm^{-1})

The tetrahedral stretching modes are present in the 900–1200 cm^{-1} spectral region. The antisymmetric stretching modes of T_2 are at 990 and 1000 cm^{-1}, and that for T_1-O-T_2 is at 1054 cm^{-1}. The mode at 1100 cm^{-1} is assigned to an antisymmetric stretching of the SiO_4 tetrahedra. The symmetric stretching modes of T_2 are at 1013 and 1029 cm^{-1}, that of T_1 at 1132 cm^{-1}, and finally at 1123 cm^{-1} that of T_1-O-T_2.

4.5 | General Considerations

Upon comparison, the frequencies of A_g modes in our study generally exhibited good agreement with those reported in Refs. [38, 39]. However, deviations were observed in certain mode frequencies. For example, the mode at 82 cm^{-1} in our study slightly differs compared to the values reported in Refs. [38, 39]. Similarly, modes 162 and 199 cm^{-1} exhibited variations between our study and previous literature.

In the case of B_g modes, our study also demonstrated consistency with frequencies reported in [38, 39], albeit with some deviations. Notably, the peak at 105 cm^{-1} showed minor differences compared to [38] (81 cm^{-1}) and [39] (109 cm^{-1}).

In [38] two unidentified modes were detected at 404 and 413 cm^{-1}, respectively. We observed only a single and equivalent activity at 408 cm^{-1}, identified as A_g mode because it manifests only along the a axes and from the tetrahedral deformations associated to the bending modes of the Al–O–Si and Si–O–Si bonds. Indeed, the outcome from SL23 model confirms our experimental result.

Ref. [38] reported as ambiguous the mode at 763 cm^{-1} due to the overlap of the 784 and 741 cm^{-1} bands possibly due to non-ideal polarization conditions effects. In our case, however, we were able to isolate and assign it to the component α of the scattering matrix, identifying the possible cause of ambiguity as a misunderstanding of the two adjacent modes (755 cm^{-1} belonging to the component β and 774 cm^{-1}, which is part of the component γ).

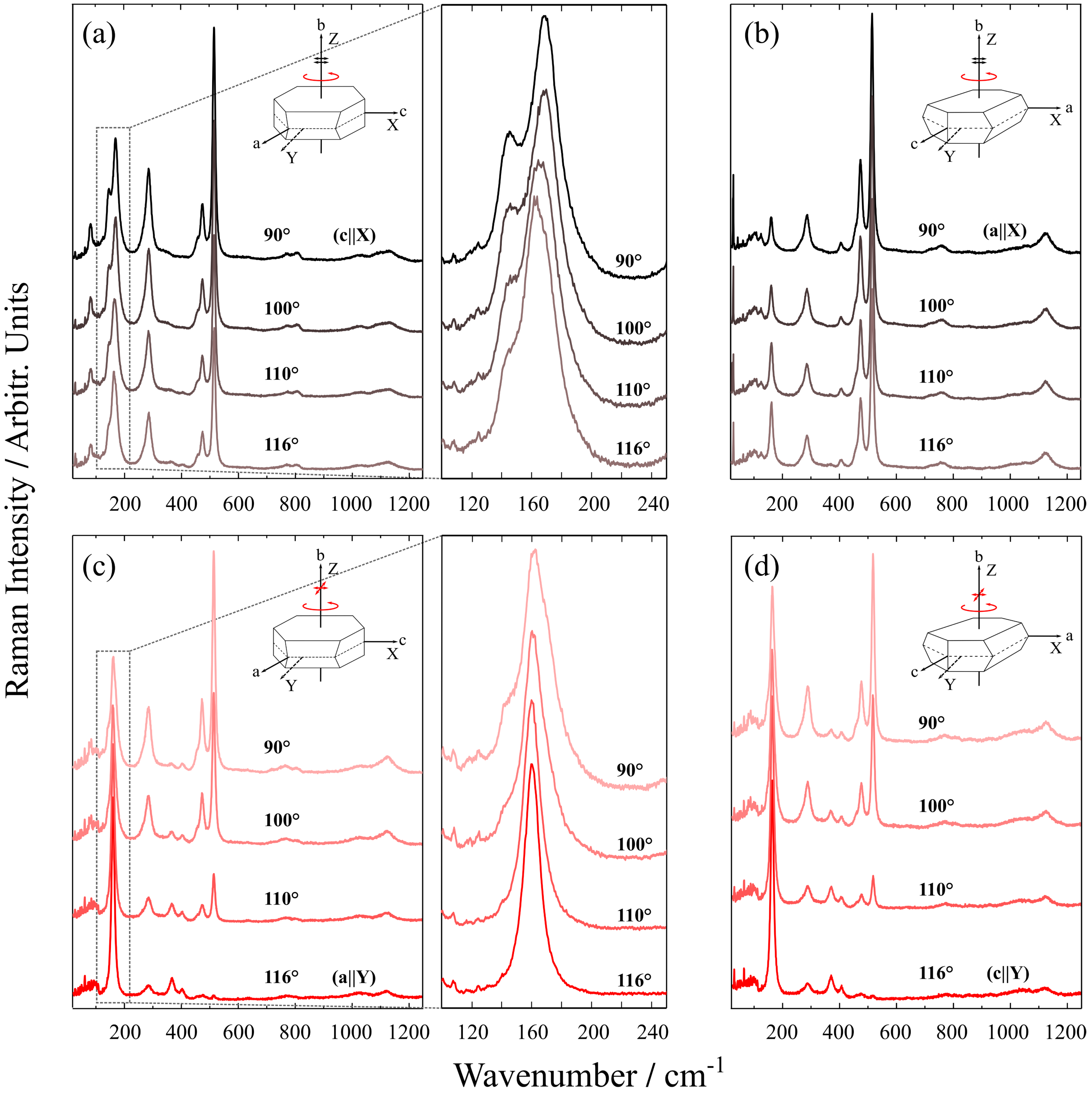

FIGURE 5 | Raman spectra of the sample measured in two polarization configurations, parallel (XX, panels a and b) and crossed (XY, panels c and d), as a function of the rotation angle in the $a - c$ plane (90°, 100°, 110°, and 116° with respect to the lab Y axis). All panels show the full-spectral range. Panels (a) and (c) include magnified views of the low-frequency region (120–240 cm^{-1}). Insets illustrate the experimental geometry and axes orientations.

This is also confirmed by the calculation obtained from the model SL23 providing as output a clear A_g mode at 759 cm^{-1}. Belonging to the Si-O-Si (thus Si-O-Al) bending modes, this frequency range is obviously and strongly influenced by the Al position that probably changes the configuration within the T_2 site. Indeed, the different models provides 5 peaks between 700 and 900 cm^{-1} consistent with the experimental spectra.

Of particular interest is the observation that the interactions between the extra-framework cations and the framework oxygen atoms in feldspars are weaker than the M–O interactions in other minerals such as olivine and pyroxene. Consequently, the Raman spectra of feldspars are not sensitive to Na and K content and do not show significant differences across such compositional ranges [19]. However, the distinctive characteristic of sanidine is the broadening of peaks in the high-frequency region, where stretching and rocking modes occur. This behavior appears to be solely attributed to the Al-Si statistical disorder. Indeed, depending on the T-site distribution within the cell, this disorder may cause a certain degree of local distortion due to the Si-O-Si and Si-O-Al bonds angular distributions [42] and introducing a certain mode selection ambiguity that challenges the assignation in this spectral range. In fact, the region in which Al occupies statistically the T site lost the mirror and diad axis to a restricted local triclinic symmetry.

4.6 | Polarization Test Within the $a - c$ Plane

To further validate the symmetry of the observed Raman-active modes, we performed a polarization test by systematically rotating the sample around its crystallographic *b*-axis. The incident laser beam was aligned along the *b*-axis (Z direction), while the scattered light was collected in backscattering geometry. Spectra were recorded in both parallel (XX) and crossed (XY) polarization configurations, varying in turn the orientation of *a* and *c* axes within the *a*–*c* plane from 90° to 116° with respect to the lab Y axis. The spectra acquired at 90° in XX and at 116° in XY correspond to those displayed in Figure 3e,f respectively. Figure 5 illustrates also the evolution of the spectral profile for both polarizations (XX and XY) as a function of the sample rotation in the $a - c$ plane, with respect to the electric field direction of incident and scattered light. In details, the top spectra of panels (a) and (b) are observed when $c \parallel$ X and $a \parallel$ X respectively. In turn, the bottom spectra of panels (c) and (d) are observed when $a \parallel$ Y and $c \parallel$ Y, respectively.

In Figure 5a, the low-frequency A_g modes (at 146 and 170 cm^{-1}) weaken drastically in favor of the B_g mode, which is observable through the apparent shift to lower wavenumbers relative to the centroid at 170 cm^{-1}. The magnified zoom shows a clear spill-over of the B_g mode at 162 cm^{-1} overlapping with the A_g mode at 170 cm^{-1} as the angle increases from 90° to 116°, noticeably altering the spectral profile. In Figure 5c, the inset shows that the spill-over of A_g into B_g results only in a marginal broadening of the band, without significantly shifting its centroid. This indicates that the selection of vibrational modes is more effective in the XY configuration than in XX, further confirming that the symmetry assignments of the observed Raman modes are reproducible and unambiguous. In Figure 5b, the A_g modes at 286, 408, 475, and 516 cm^{-1} remain almost invariant with rotation, while a slight increase in the relative intensity of the B_g mode at 162 cm^{-1} is observed as the angle varies from 90° to 116°. Indeed, Figure 5d highlights that the A_g modes progressively vanish, and the B_g modes significantly intensify from 90° to 116°, as theoretically expected. These results suggest that the slight misalignment of the crystallographic axes does not compromise the symmetry-based analysis. While the spectra are never perfectly polarized along both axes simultaneously, they remain selectively polarized along one axis at a time. Overall, these results demonstrate that the polarization-dependent analysis is robust and reliable, even in the presence of minor angular deviations or non-ideal experimental conditions.

5 | Conclusion

By combining polarized Raman spectra measured on oriented crystals with ab initio calculations we derived a full assignment of the normal modes for sanidine. Polarized spectra were acquired in six different scattering geometries, obtaining excellent agreement with the predictions of the Raman tensor.

Conducting ab initio calculation at DFT level of theory employing different functionals, namely PBE, PBEsol, and PBE0, we demonstrated that the inclusion of Hartree-Fock exchange in PBE0 enhances the accuracy of wave number evaluations. This improvement facilitates the validation of experimentally derived assignments and assists in the assignment of normal modes, thereby resolving several previously unresolved issues cited in the literature.

Moreover, we found that models SL2 and SL3 in which Al is located in T_1 site are slightly more stable than SL1 and SL4, in which Al is located at the T_2 site. The Raman spectra differences align best between calculated vibrational wavenumbers and measurements for models SL2 and SL3.

X-ray diffraction produces an average sanidine crystal structure in which T_2 sites are closer than T_1 sites, with Al disordered at both sites. The disordered model also accounts for the Loewenstein Al-avoidance rule, which prohibits direct Al^{IV}-O-Al^{IV} linkages.

The current models of sanidine-orthoclase-microcline phase transitions suggest that during transformation Al migrates from T_2 to orders in T_1 since the latter becomes energetically favorable decreasing temperature [8–10].

In our sanidine models the energy associated to Al distribution at T_1 and T_2 tetrahedral sites is comparable, thought not identical, with a preference of Al for T_1.

The order–disorder processes, being driven by the kinetics of the reaction, provide useful information about the long-term thermal history of host-rocks. Our results thus provide a further theoretical insight into the model for the K-feldspar order–disorder phase transition, which is very slow and impossible to achieve in the laboratory. In addition to the results derived from our investigation into this complex system, a comprehensive effort in the assignment of normal modes can be leveraged not only for the identification of sanidine samples but also for the analysis of the K-feldspar phase transition via Raman spectroscopy.

Author Contributions

Michele Cassetta: conceptualization, methodology, validation, visualization, writing – original draft. **Luca Bellucci:** methodology, validation, data curation, writing – original draft. **Sabrina Nazzareni:** methodology, validation, data curation, writing – original draft. **Francesco Vetere:** methodology, data curation, writing – review and editing. **Marco Giarola:** methodology, data curation, writing – review and editing. **Gino Mariotto:** methodology, validation, resources, data curation, funding acquisition, writing – review and editing.

Acknowledgments

This study was supported by the following: L.B.: Project PRIN 2022–Cod. 202278NHAM (PE11) CHERICH-C "Chemical and electrochemical energy storage materials from organic wastes: the treasure hidden in C based materials"–CUP B53D23008590006, funded by the European Union–Next Generation EU in the context of the Italian National Recovery and Resilience Plan, Mission 4, Component 2, Investment 1.1, "Fondo per il Programma Nazionale di Ricerca e Progetti di Rilevante Interesse Nazionale (PRIN)"; M.C., M.G., and G.M.: European Union's Horizon 2020 research and innovation program under Grant agreement No. 689868; F.V.: Piano di Sostegno alla Ricerca 2022 per finanziamenti a progetti di ricerca Curiosity-driven (UniSi, F-CUR CREAMI). M.C. lovely dedicates this work to Iris and Marilisa. Open access publishing facilitated by Universita degli Studi di Verona, as part of the Wiley - CRUI-CARE agreement.

Conflicts of Interest

The authors declare no conflicts of interest.

Data Availability Statement

The data that support the findings of this study are available from the corresponding author upon reasonable request.

References

1. W. L. Brown and I. Parsons, "Towards a More Practical Two-Feldspar Geothermometer," *Contributions to Mineralogy and Petrology* 76, no. 4 (1981): 369–377.

2. I. Parsons, *Feldspars and Their Reactions*, vol. 421, (Springer Science & Business Media, 2012).

3. H. Chengcheng and H. Li, "A Revisit to the Phase Transition Behavior of K-Feldspar at High-Pressure and High-Temperature: Implications on Metastable K-Feldspar in Cold Subduction," *American Mineralogist* 109, no. 3 (2024): 439–448.

4. F. Tutti, L. S. Dubrovinsky, S. K. Saxena, and S. Carlson, "Stability of $KAlSi_3O_8$ Hollandite-Type Structure in the Earth's Lower Mantle Conditions," *Geophysical Research Letters* 28, no. 14 (2001): 2735–2738.

5. R. Trønnes, "Stability Range and Decomposition of Potassic Richterite and Phlogopite End Members at 5–15 GPa," *Mineralogy and Petrology* 74 (2002): 129–148.

6. S. Nazzareni, P. Comodi, L. Bindi, G. Garbarino, and A. Bobrov, "Equation of State of Fe^{3+}-Bearing Phase-X," *Physics and Chemistry of Minerals* 39 (2012): 553–559.

7. M. W. Phillips and P. H. Ribbe, "The Structures of Monoclinic Potassium-Rich Feldspars," *American Mineralogist* 58, no. 3–4 (1973): 263–270.

8. E. Salje, "Thermodynamics of Sodium Feldspar I: Order Parameter Treatment and Strain Induced Coupling Effects," *Physics and Chemistry of Minerals* 12, no. 2 (1985): 93–98.

9. E. Salje, "Thermodynamics of Sodium Feldspar II: Experimental Results and Numerical Calculations," *Physics and Chemistry of Minerals* 12, no. 2 (1985): 99–107.

10. E. Salje, "Raman Spectroscopic Investigation of the Order Parameter Behavior of Hypersolvus Alkali Feldspar: Displacive Phase Transition and Evidence of Na–K Site Ordering," *Physics and Chemistry of Minerals* 13, no. 5 (1985): 340–346.

11. P. H. Ribbe, "A Refinement of the Crystal Structure of Sanidinized Orthoclase," *Acta Crystallographica* 16, no. 5 (1963): 426–427.

12. M. Murri, F. Cámara, J. Adam, M. Domeneghetti, and M. Alvaro, "Intracrystalline "Geothermometry" Assessed on Clino and Orthopyroxene Bearing Synthetic Rocks," *Geochimica et Cosmochimica Acta* 227 (2018): 133–142.

13. H. Kroll and R. Knitter, "Al, Si Exchange Kinetics in Sanidine and Anorthoclase and Modeling of Rock Cooling Paths," *American Mineralogist* 76, no. 5–6 (1991): 928–941.

14. M. Murri, M. C. Domeneghetti, A. M. Fioretti, et al., "Cooling History and Emplacement of a Pyroxenitic Lava as Proxy for Understanding Martian Lava Flows," *Scientific Reports* 9, no. 1 (2019): 17051.

15. S. Nazzareni, V. Barbarossa, H. Skogby, V. Zanon, and M. Petrelli, "Magma Water Content of Pico Volcano (Azores Islands, Portugal): A Clinopyroxene Perspective," *Contributions to Mineralogy and Petrology* 175 (2020): 1–16.

16. S. Nazzareni, H. Skogby, and P. F. Zanazzi, "Hydrogen Content in Clinopyroxene Phenocrysts From Salina Mafic Lavas (Aeolian Arc, Italy)," *Contributions to Mineralogy and Petrology* 162 (2011): 275–288.

17. S. Nazzareni, D. Morgavi, M. Petrelli, O. Bartoli, and D. Perugini, "Magmatic Processes at Euganean Hills (Veneto Volcanic Province, Italy): Clinopyroxene Investigation to Unravel Magmatic Interactions," *Geosciences* 12, no. 3 (2022): 108.

18. T. P. Mernagh, "Use of the Laser Raman Microprobe for Discrimination Amongst Feldspar Minerals," *Journal of Raman Spectroscopy* 22 (2009): 453–457.

19. J. J. Freeman, A. Wang, K. E. Kuebler, B. L. Jolliff, and L. A. Haskin, "Characterization of Natural Feldspars by Raman Spectroscopy for Future Planetary Exploration," *Canadian Mineralogist* 46, no. 6 (2008): 1477–1500.

20. G. Anbalagan, G. Sankari, S. Ponnusamy, R. T. Kumar, and S. Gunasekaran, "Investigation of Silicate Mineral Sanidine by Vibrational and NMR Spectroscopic Methods," *Spectrochimica Acta Part A: Molecular and Biomolecular Spectroscopy* 74 (2009): 404–409.

21. P. Makreski, G. Jovanovski, and B. Kaitner, "Minerals From Macedonia. XXIV. Spectra-Structure Characterization of Tectosilicates," *Journal of Molecular Structure* 924–926, no. C (2009): 413–419.

22. M. Cassetta, B. Rossi, S. Mazzocato, et al., "Deep-UV Raman Spectroscopy: A Novel Heuristic Method to Characterize Volcanologically Relevant Glasses on Mars," *Chemical Geology* 644 (2024): 121867.

23. M. Cassetta, G. Mariotto, N. Daldosso, et al., 2023. "Viscosity, Boson Peak and Elastic Moduli in the Na_2O-SiO_2 System. *Minerals* 13, no. 9: 1166, https://doi.org/10.3390/min13091166.

24. M. Giarola, A. Sanson, F. Monti, et al., "Vibrational Dynamics of Anatase TiO_2: Polarized Raman Spectroscopy and Ab Initio Calculations," *Physical Review B* 81 (2010): 1–7.

25. T. C. Damen, S. P. S. Porto, and B. Tell, "Raman Effect in Zinc Oxide," *Physical Review* 142, no. 2 (1966): 570–573.

26. J. Hutter, M. Iannuzzi, F. Schiffmann, and J. VandeVondele, “CP2K: Atomistic Simulations of Condensed Matter Systems,” *Wiley Interdisciplinary Reviews: Computational Molecular Science* 4, no. 1 (2014): 15–25.

27. T. D. Kühne, M. Iannuzzi, M. Del Ben, et al., “CP2K: An Electronic Structure and Molecular Dynamics Software Package-Quickstep: Efficient and Accurate Electronic Structure Calculations,” *Journal of Chemical Physics* 152, no. 19 (2020): 194103.

28. J. VandeVondele, M. Krack, F. Mohamed, M. Parrinello, T. Chassaing, and J. Hutter, “Quickstep: Fast and Accurate Density Functional Calculations Using a Mixed Gaussian and Plane Waves Approach,” *Computer Physics Communications* 167, no. 2 (2005): 103–128.

29. S. Goedecker, M. Teter, and J. Hutter, “Separable Dual-Space Gaussian Pseudopotentials,” *Physical Review B* 54 (1996): 1703–1710, https://doi.org/10.1103/PhysRevB.54.1703.

30. C. Hartwigsen, S. Goedecker, and J. Hutter, “Relativistic Separable Dual-Space Gaussian Pseudopotentials From H to Rn,” *Physical Review B* 58 (1998): 3641–3662, https://doi.org/10.1103/PhysRevB.58.3641.

31. J. P. Perdew, K. Burke, and M. Ernzerhof, “Generalized Gradient Approximation Made Simple [Phys. Rev. Lett. 77, 3865 (1996)],” *Physical Review Letters* 78 (1997): 1396, https://doi.org/10.1103/PhysRevLett.78.1396.

32. J. P. Perdew, A. Ruzsinszky, G. I. Csonka, et al., “Restoring the Density-Gradient Expansion for Exchange in Solids and Surfaces,” *Physical Review Letters* 100 (2008): 136406, https://doi.org/10.1103/PhysRevLett.100.136406.

33. J. P. Perdew, M. Ernzerhof, and K. Burke, “Rationale for Mixing Exact Exchange With Density Functional Approximations,” *Journal of Chemical Physics* 105, no. 22 (1996): 9982–9985.

34. S. Grimme, J. Antony, S. Ehrlich, and H. Krieg, “A Consistent and Accurate *Ab Initio* Parametrization of Density Functional Dispersion Correction (DFT-D) for the 94 Elements H-Pu,” *Journal of Chemical Physics* 132, no. 15 (2010): 154104.

35. M. Guidon, J. Hutter, and J. VandeVondele, “Robust Periodic Hartree-Fock Exchange for Large-Scale Simulations Using Gaussian Basis Sets,” *Journal of Chemical Theory and Computation* 5, no. 11 (2009): 3010–3021.

36. M. Guidon, J. Hutter, and J. VandeVondele, “Auxiliary Density Matrix Methods for Hartree-Fock Exchange Calculations,” *Journal of Chemical Theory and Computation* 6, no. 8 (2010): 2348–2364.

37. J. Deubener, M. Sternitzke, and G. Müller, “Feldspars MAlSi$_3$O$_8$ (M = H, Li, Ag) Synthesized by Low-Temperature Ion Exchange,” *American Mineralogist* 76, no. 9–10 (1991): 1620–1627.

38. V. P. Vodop'yanova, A. P. Mirgorodskii, and A. N. Lazarev, “Raman Spectra of Potassium Feldspars,” *Inorganic Materials* 20 (1984): 1667–1674.

39. M. O. von Stengel, “Normalscliwingungen von Alkalifeldspäten,” *Zeitschrift Für Krist* 146, no. 1-3 (1977): 1–18.

40. D. W. Matson, S. K. Sharma, and J. A. Philpotts, “Raman-Spectra of Some Tectosilicates and of Glasses Along the Orthoclase-Anorthite and Nepheline-Anorthite Joins,” *American Mineralogist* 71 (1986): 694–704.

41. B. Velde and H. Boyer, “Raman Microprobe Spectra of Naturally Shocked Microcline Feldspars,” *Journal of Geophysical Research: Solid Earth* 90, no. B5 (1985): 3675–3681.

42. D. A. McKeown, “Raman Spectroscopy and Vibrational Analyses of Albite: From 25°C Through the Melting Temperature,” *American Mineralogist* 90 (2005): 1506–1517.

Supporting Information

Additional supporting information can be found online in the Supporting Information section. **Supporting Information S1:** The supplementary material covers comprehensive details of ab initio calculations, cell parameters, and energy per atom, as well as simulated Raman spectra and visualization of normal modes. **Table S1:** Cell parameters. **Table S2:** Energy per atoms values for all the modes and PBE, PBEsol, and PBE0 functionals. **Figure S1:** Reconstructed Raman spectra for all models and functionals. For each wavenumber, a Lorentzian function is applied, where the peak represents the Raman intensity and the full width at half maximum (FWHM) is consistently set to 12 cm−1. **Figure S2:** Reconstructed Raman spectra utilizing the PBE0 functional. **Figure S3:** Comparison between the total experimental Raman spectrum (vertically shifted for clarity) and the reconstructed Raman spectra obtained using the PBE0 functional for models SL23 (black) and SL14 (red). Notably, the most intense peak around 516 cm^{-1} appears in all spectra and shows good agreement between experiment and simulations. At higher frequencies, models SL1 and SL4 diverge more significantly, particularly around 1200 cm^{-1}, where a peak is present in SL1 and SL4 but completely absent in both the experimental Raman spectrum and the SL2 and SL3 calculated spectra. **Table S3:** Selected calculated normal modes. **Table S4:** List of assigned normal modes (ANMs) and comparison of calculated vibrational modes for the SL2 and SL3 models with experimental data. According to factor group analysis, sanidine exhibits 75 optical modes. However, the CP2K software used for geometry optimization and vibrational analysis does not impose symmetry constraints and treats the unit cell as primitive. As a consequence, the vibrational modes calculated after minimization deviate from the ideal $C2/m$ space group symmetry, as no symmetry constraints were applied during the relaxation of structures in which aluminum atoms were explicitly placed (see Section 2.4 “Modeling and Computational Details” and Figure 3 in the main text). This symmetry reduction lifts degeneracies and leads to the appearance of additional modes, increasing the total number well beyond the 75 expected from group theory, up to 153. The top left column lists the indices of the calculated normal modes, with symmetry assignments indicated in parentheses. These assignments were made qualitatively by inspecting the symmetry properties of the individual displacement vectors, as shown in the two right-hand columns for the SL2 and SL3 models, respectively. Symmetries marked with “()*” are provisional (i.e., not rigorously assigned) and are based on a subset of vectors that qualitatively conform to expected symmetry operations. At the bottom of the table, the experimental wavenumbers with their assigned symmetry labels are also reported.